Contrasting Hydrodynamic Responses to Atmospheric Systems with Different Scales: Impact of Cold Fronts vs. That of a Hurricane

Wei Huang [1],* and **Chunyan Li** [2]

[1] Virginia Institute of Marine Science, College of William and Mary, Gloucester Point, VA 23062, USA

[2] Department of Oceanography and Coastal Sciences, School of Coast and Environment, Louisiana State University, Baton Rouge, LA 70803, USA; cli@lsu.edu

* Correspondence: whuang@vims.edu

Abstract: In this paper, subtidal responses of Barataria Bay to an atmospheric cold front in 2014 and Hurricane Barry of 2019 are studied. The cold fronts had shorter influencing periods (1 to 3 days), while Hurricane Barry had a much longer influencing period (about 1 week). Wind direction usually changes from southern quadrants to northern quadrants before and after a cold front's passage. For a hurricane making its landfall at the norther Gulf of Mexico coast, wind variation is dependent on the location relative to the location of landfall. Consequently, water level usually reaches a trough after the maximum cold front wind usually; while after the maximum wind during a hurricane, water level mostly has a surge, especially on the right-hand side of the hurricane. Water level variation induced by Hurricane Barry is about 3 times of that induced by a cold front event. Water volume flux also shows differences under these two weather types: the volume transport during Hurricane Barry was 4 times of that during a cold front. On the other hand, cold front events are much more frequent (30–40 times a year), and they lead to more frequent exchange between Barataria Bay and the coastal ocean.

1. Introduction

The coast of Louisiana in the northern Gulf of Mexico (NGOM) is characterized by semi-enclosed bays with exchange flows of water through multiple inlets, such as Lake Pontchartrain, Calcasieu Lake, Vermillion Bay, and Barataria Bay. They have limited connections with the coastal ocean except through narrow inlets. These are, however, different from inland freshwater lakes or general coastal plain estuaries connected to the coastal ocean through multiple inlets. The NGOM has several major environmental processes that are determined by hydrodynamics, particularly those related to the exchange of water and sediment between estuaries and shelf water, e.g., the significant land loss around lower Mississippi River basin associated with processes that cause erosion and sediment transport [1–6]. Along the NGOM coast, the most regular hydrodynamic motions are the relatively weak tides, which are mainly diurnal oscillations with a maximum tidal range of about 0.6 m [7,8]. Because of weak tides, the effect of weather [9–14] becomes more prominent in moving the sediment through inundation and erosion [15]. As a result, the less predictable weather-induced bay oscillations may cause more significant flood and drain of the micro-tidal system [16–20]. Synoptic weather systems and hurricanes can produce responses in these water bodies affecting the water exchange, which is important to the ecosystem [21–23]. However, there is a lack of in-depth analysis of weather conditions characterizing different weather patterns.

Among the weather influences, hurricane impact can be most dramatic. Because of the low gradient of land and relatively shallow and broad shelf along NGOM, hurricanes can cause significant damages to the micro-tidal coast zone [24–28]. For instance, severe storm surge caused damages in 2005 by Hurricanes Katrina and Rita [29–33], in 2008 by Hurricanes Gustav and Ike [34–37], and in 2017 by Hurricanes Harvey and Irma [38]. Compared with hurricanes, cold front-associated winds can be more frequent, and have a more accumulative effect in driving the hydrodynamics. The length of influence of a cold front can reach ~2000–3000 km, much larger [39] than the region of strong wind within a typical hurricane. Previous studies have covered various aspects of weather impact to coastal ocean. For example, Keen [40] used numerical models to predict the waves and currents under cold front passage over Mississippi bight. Keen and Stavn [41] later used observations and numerical models with interaction of atmospheric forcing and hydrodynamics to investigate the optical environment at Santa Rosa Island, Florida during two cold front passages. Water exchange and circulations in the bays and estuaries under meso-scale weather systems like winter storms and cold fronts can be related not only to the circulations in the coastal regions but also to the sediment transport [42] and ecosystems. Sediment transport and distributions on the shallow shelf and in the estuaries of Gulf of Mexico under the influence of cold front passages in winter time are investigated by, e.g., Perez et al. [43] and Kineke et al. [44]. Siadatmousavi et al. [45] studied the wave energy during a cold front and skill assessed a phase-averaged spectral wave model.

There have been many studies on subtidal flow in estuaries [46–48]. In these studies, the wind effects are often discussed as a time series forcing without examining the spatial structure of the weather systems. The subtidal energy in the estuarine circulations caused by cold fronts may be comparable if not larger than that of tides in the area [49]. A recent study [50] investigated the weather-induced exchange flows through multiple inlets of the Barataria Bay in a few months period in 2013, 2014, and 2015 with 51 atmospheric cold fronts passing the Louisiana coast. These events are apparently very common: an analysis [51] covering a period of 40 years identified more than 1600 atmospheric frontal events, with an average of ~41.2 ± 4.7 per year excluding the months between May and August for much weaker activities of this kind. However, no quantitative comparisons are made between the hydrodynamic responses induced by cold fronts and that from hurricanes. Therefore, it is of interest for a comparison between the hydrodynamic responses to these two different weather systems with different scales.

This work will use a calibrated three-dimensional finite volume community model (FVCOM) to simulate water level and flows in Barataria Bay under multi-scale weather systems including cold front and hurricane events. The goals are to (1) compare the hydrodynamic responses to different weather systems (cold front and hurricane), (2) examine water exchange between Barataria Bay and coastal ocean through multiple inlets under the different weather systems, and (3) assess the quasi-steady state balance under different weather systems.

2. Study Site and Data

Barataria Bay (Figure 1) is a shallow estuary in southeast Louisiana and south of the City of New Orleans. It is bounded by several barrier islands and irregular-shaped wetlands with multiple tidal inlets connecting to the open ocean. The main axis from north to south and from east to west is about 30–40 km. The tidal inlets include Barataria Pass with a width of ~800 m and a maximum depth of 20 m at the mouth, Caminada Pass with ~800 m width, 9 m depth, and a 90 degree turn in channel orientation near the mouth, and the 15 m deep Pass Abel with a width of about 1.9 km. Freshwater is mainly from the manmade Davis Pond Diversion facility with a capacity of about 250 m^3/s of flux. Water inside the Barataria Bay is very shallow (average depth of 2 m). Erosions in the bay appear to be significant, e.g., there is a 50 m hole [50] northwest of the Barataria Pass, which is the deepest point among all Louisiana lagoons, bays, and estuaries, revealing the significant contribution of non-tidal forcing to the micro-tidal system.
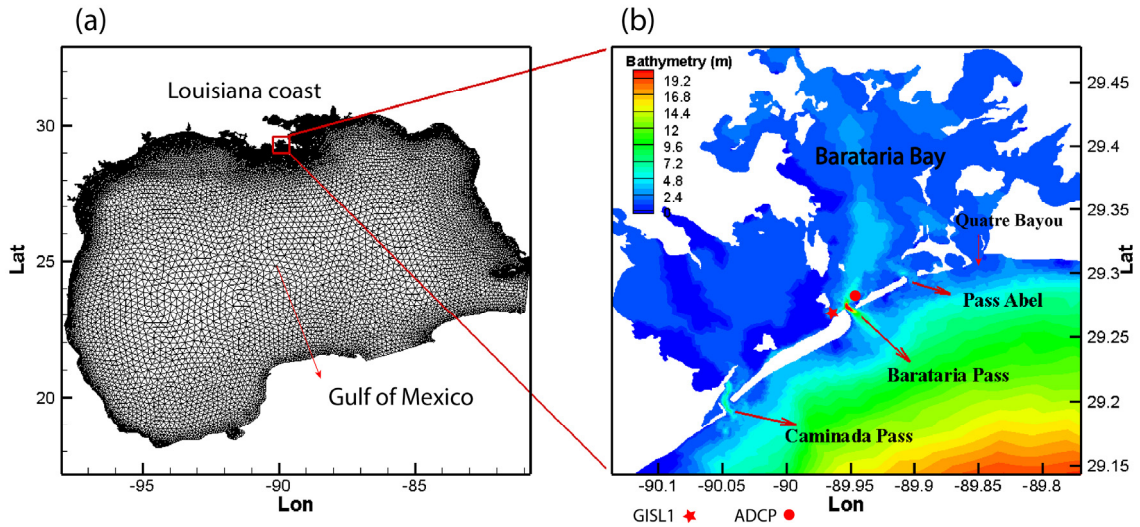
Figure 1. Study site (**b**) and model grid (**a**) for FVCOM simulation. Star represents the location of wind observations (NDBC station GISL1); red dot represents the location of ADCP deployment for water level and velocity observations.

Observational data of water level and velocity were obtained from 5 Sontek Argonaut DP SL 500-KHz horizontal acoustic Doppler current profilers (ADCPs, manufacture: SonTek/Xylem Inc., San Diego, USA). Information about the measurements can be found in Li et al. [50]. Wind data are from the National Ocean Service station at Grand Isle (29.265° N, 89.958° W, Figure 1). The atmospheric forcing for the upper boundary of the hydrodynamic numerical model was obtained from the global Climate Forecast System Reanalysis (CFSR) data (https://climatedataguide.ucar.edu/climate-data/climate-forecast-system-reanalysis-cfsr).

3. Model Setup and Validation

3.1. Model Description

A finite volume community ocean model (FVCOM) was applied in this study. FVCOM is widely used for investigating coastal ocean hydrodynamics with complicated topography [52]. The governing equations are [52]:

$$\frac{\partial u}{\partial t} + u\frac{\partial u}{\partial x} + v\frac{\partial u}{\partial y} + w\frac{\partial u}{\partial z} - fv = -\frac{1}{\rho_0}\frac{\partial P}{\partial x} + \frac{\partial}{\partial z}\left(K_m\frac{\partial u}{\partial z}\right) + F_u, \tag{1}$$

$$\frac{\partial v}{\partial t} + u\frac{\partial v}{\partial x} + v\frac{\partial v}{\partial y} + w\frac{\partial v}{\partial z} + fu = -\frac{1}{\rho_0}\frac{\partial P}{\partial y} + \frac{\partial}{\partial z}\left(K_m\frac{\partial v}{\partial z}\right) + F_v, \tag{2}$$

$$\frac{\partial w}{\partial t} + u\frac{\partial w}{\partial x} + v\frac{\partial w}{\partial y} + w\frac{\partial w}{\partial z} = -\frac{1}{\rho_0}\frac{\partial p}{\partial z} + \frac{\partial}{\partial z}\left(K_m\frac{\partial w}{\partial z}\right) + F_w - g, \tag{3}$$

$$\frac{\partial u}{\partial x} + \frac{\partial v}{\partial y} + \frac{\partial w}{\partial z} = 0, \tag{4}$$

where x, y, z are the three axes in the east, north, and vertical directions, respectively; u, v, w are the x, y, z velocities, respectively, ρ_0 is the density; P is the total pressure of air and water; f is the Coriolis parameter; g is the gravitational acceleration; K_m is the vertical eddy diffusion coefficient, determined by the Mellor and Yamada [53] level-2.5 (MY-2.5) turbulent closure scheme; F_w is the diffusion term of the vertical momentum; and F_u, F_v are the diffusion terms for the horizontal momentums.

The surface and bottom boundary conditions are:

$$K_m\left(\frac{\partial u}{\partial z}, \frac{\partial v}{\partial z}\right) = \frac{1}{\rho_0}\left(\tau_{sx}, \tau_{sy}\right), \ w = \frac{\partial \zeta}{\partial t} + \frac{\partial \zeta}{\partial x} + \frac{\partial \zeta}{\partial y}, \ at \ z = \zeta(x, y, t), \tag{5}$$

$$K_m\left(\frac{\partial u}{\partial z}, \frac{\partial v}{\partial z}\right) = \frac{1}{\rho_0}\left(\tau_{sx}, \tau_{sy}\right), \ w = -u\frac{\partial H}{\partial x} - v\frac{\partial H}{\partial y}, \ at \ z = -H(x, y), \tag{6}$$

where $\left(\tau_{sx}, \tau_{sy}\right)$ and $\left(\tau_{bx}, \tau_{by}\right)$ are the surface wind stress and bottom stress vectors, respectively. H is the water depth and ζ is the surface elevation. $\left(\tau_{sx}, \tau_{sy}\right)$ is calculated by $C_d\rho_a|U_{10}|U_{10}$, where U_{10} is the wind at 10 m height, ρ_a is the air density (1.29 kg/m^3), and C_d is the surface wind drag coefficient and is calculated by the following equations:

$$C_d = \begin{cases} (0.49 + 0.065 \times 11.0) \times 10^{-3}, \ U_{10} < 11.0 \ m/s \\ (0.49 + 0.065 \times |U_{10}|) \times 10^{-3}, \ 11.0\frac{m}{s} \leq U_{10} \leq 25.0 \ m/s \\ (0.49 + 0.065 \times 25.0) \times 10^{-3}, \ U_{10} > 25.0 \ m/s \end{cases}, \tag{7}$$

where $\left(\tau_{bx}, \tau_{by}\right)$ is the bottom stress calculated by $C_d\sqrt{u^2 + v^2}(u, v)$, where C_d is the drag coefficient and is determined by the following equation:

$$C_d = \max\left(\frac{k^2}{\ln\left(\frac{z_{ab}}{z_0}\right)^2}, 0.0025\right), \tag{8}$$

where k is the von Karman constant (0.4), z_0 is the bottom roughness parameter, and z_{ab} is the height above the bottom.

3.2. Model Setup

The model mesh covers the entire Gulf of Mexico, horizontally from 80.7° W to 97.9° W, and zonally from 18.1° N to 30.7° N (Figure 1). There are two open boundaries. One is located in the Caribbean Sea, connecting the east border of the Mexico and the west edge of Cuba. The other open boundary is located at the North Atlantic Ocean with the north point in the edge of Florida and the south point at the border of Cuba. The mesh contains 119,566 nodes and 214,297 elements. The finest resolution is about 50 m. There are 40 sigma layers. The model is three-dimensional barotropic, so salinity and temperature are not simulated nor discussed. The model is cold started with a time step of 1 s. The output time interval is set to be 30 min. The time periods for cold fronts and Hurricane Barry are from 20 December 2013 to 30 January 2014 and 20 June to 30 July 2019, respectively. Open boundary is only forced by tides, a combination of 10 tidal constituents (M2, S2, N2, K2, K1, O1, P1, Q1, MF, and MM). It is predicted by a tide model called TMD [54]. Wind stress and air pressure at mean sea level forcing at surface are obtained from the global Climate Forecast System Reanalysis (CFSR: https://climatedataguide.ucar.edu/climate-data/climate-forecast-system-reanalysis-cfsr) data with horizontal resolution of 0.5 degree by 0.5 degree.

3.3. Model Validation

The skill scores of FVCOM in simulating water elevation and along-channel velocity are 0.7 and 0.67 (Figure 2), which shows "excellent" performance based on Wu et al. [55]. The low-pass filtered water elevation and velocity are also in line with the observed data, which are categorized as "very good" with the skill scores of 0.51 and 0.60 (Figure 2). Discrepancies between the modeled and observed low-pass filtered water levels and along channel velocities may be caused by the uncertainty of bathymetry of these highly active tidal inlets. As mentioned earlier, tidal passes of Barataria bay are severely eroded. The model bathymetry may therefore have errors, leading to larger uncertainties in

model results. Since our focus is on the weather-induced hydrodynamics, variables to be examined below are all low-pass filtered with a cut off frequency of 0.6 cycles per day.
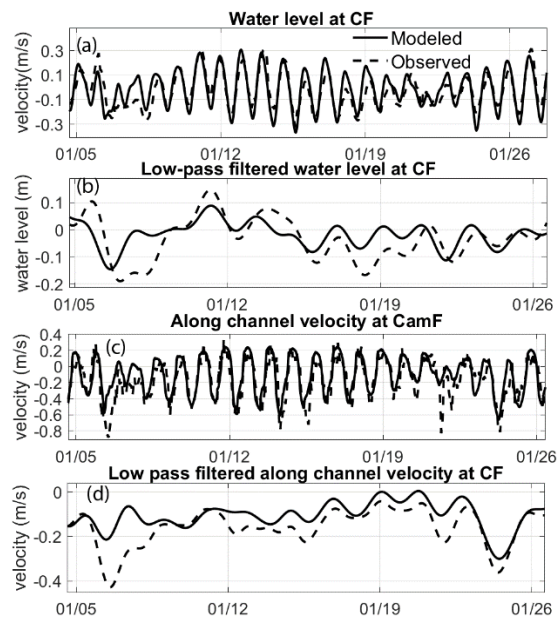

Figure 2. Validation of water level and along-channel velocity using observation in January 2014 at Caminada Pass, (**a,c**) are validations of water elevation and surface flow at Caminada Pass, (**b,d**) are validations of low-pass filtered water elevation and along channel velocity at Caminada Pass. Skill score for water level and along channel simulation are 0.7 and 0.67, which are categorized as "excellent".

3.4. Atmospheric Background

Here, we examine two types of atmospheric systems with different scales and influence regions. One is a cold front that entered the study area around 0000 UTC, 6 January 2014 and left the region around 1800 UTC, 6 January 2014. As shown in Figure 3a,b, the cold front developed from a low-pressure center (1003 hPa), which was located in Indiana. Southwesterly wind was dominating in our study site. As the front moved to the east, air pressure continued to drop to a minimum of 992 hPa. When the front was passing Barataria Bay, the southwesterly wind abruptly changed to northwesterly wind. After the cold front's passage, wind was from the northern quadrants for about two days with a maximum magnitude of 13.5 m/s (Figure 4a). This cold front passage is a typical weather phenomenon between late fall and the following spring (mostly October to April). During each of the frontal events, wind changes its direction from southern quadrants to northern quadrants when the cold front passages [50].

The other type of weather system studied here is Hurricane Barry. Hurricane Barry was first originated from a mesoscale convective vortex on 2 July 2019. It went into Gulf of Mexico on 10 July and developed into a tropical depression, before being upgraded to Tropical Storm Barry. It made its landfall on 13 July on Marsh Island, Louisiana, 190 km west of Barataria Bay as a Category 1 hurricane with a minimum sea-level pressure of 993 hPa and a maximum wind speed of 33 m/s (Figure 3c,d). The maximum wind speed measured at the Grand Isle station near Barataria Bay reached 14.5 m/s. Before Barry's landfall, northerly wind was dominating, and after the landfall of Barry, wind changed its direction to southerly wind and persisted for at least 4 days. From Figure 4b, one can see that Hurricane Barry had longer influencing period than the cold front mentioned above. Wind magnitude was also larger than that during the cold front.
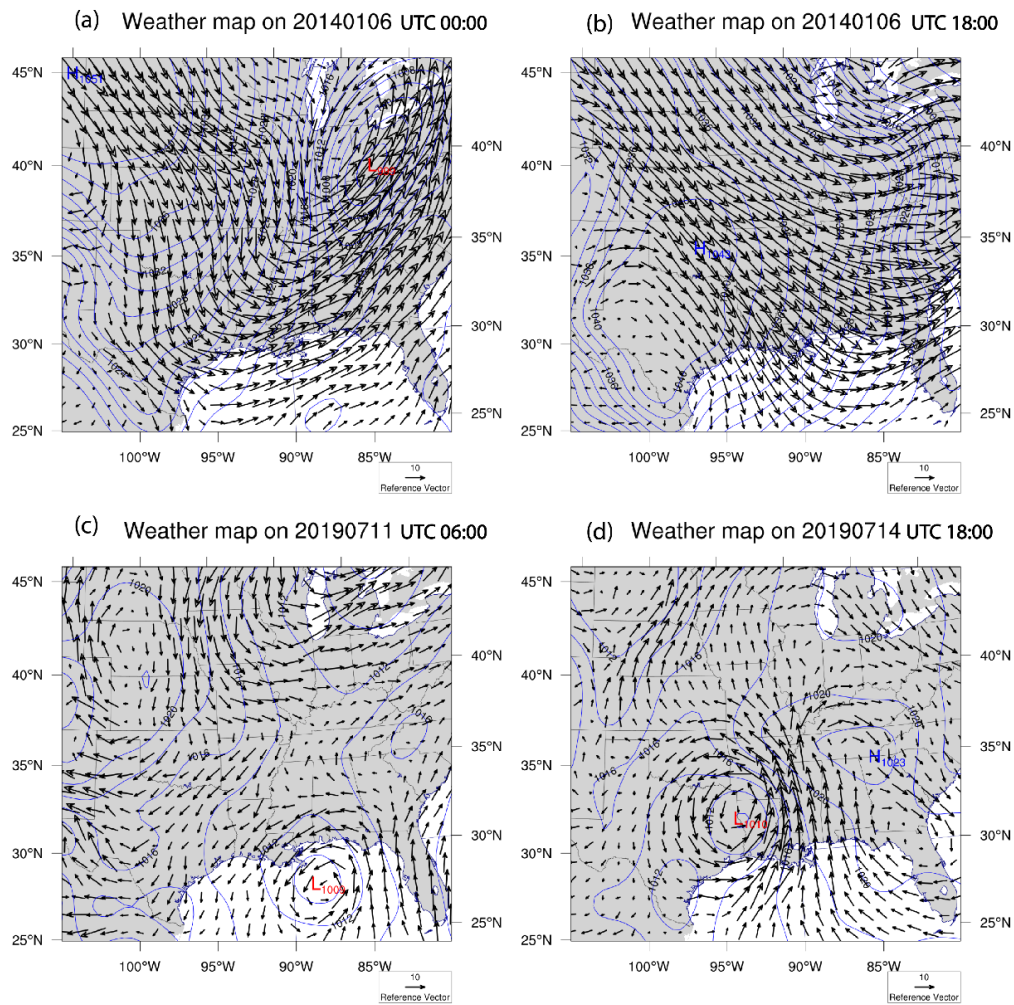
Figure 3. Weather maps during the cold front at 0000 UTC, 01/06 and 1800 UTC, 01/06, and during Hurricane Barry at 0600, 07/11 and 1800, 07/14. (**a**,**b**) are the weather maps before and after the cold front passage in January 2014, and (**c**,**d**) are weather maps before and after the landfall of Hurricane Barry. Blue lines are contours of air pressure.
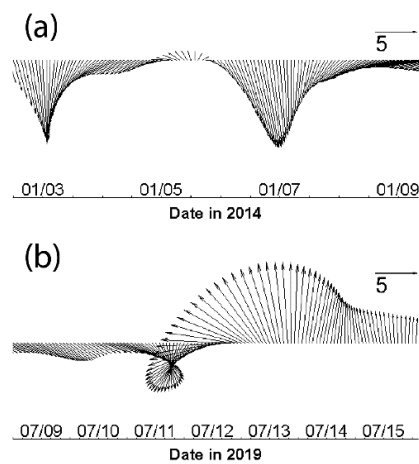

Figure 4. Wind vectors during cold front event in January 2014 and Hurricane Barry in July 2019. (max wind magnitude: 13.5 m/s and 14.5 m/s). (**a**,**b**) show the wind vectors during cold front and hurricane, respectively.

4. Results

4.1. Hydrodynamic Response

Low-pass filtered water level variations during cold front and hurricane are shown in Figure 5a,b, respectively. Water level dropped about 15 cm after the cold front passage during northerly wind, so that one can see an obvious trough at 1500 UTC on 6 January. This is because northerly wind after the cold front passage continuously blew the water out of the bay, leading to the water level minimum. As northerly wind weakened, water level begun to rise. On the other hand, when the water level was under the influence of Hurricane Barry, it is found that there was a surge of 40 cm after the hurricane's landfall, when wind also reached the maximum of 14.5 m/s. The surge resulted from the southerly wind after Barry's landfall, which blew the water from the coastal ocean into the bay. Compared with the trough induced by the cold front, the surge caused by Hurricane Barry is about 3 times larger in terms of magnitude.
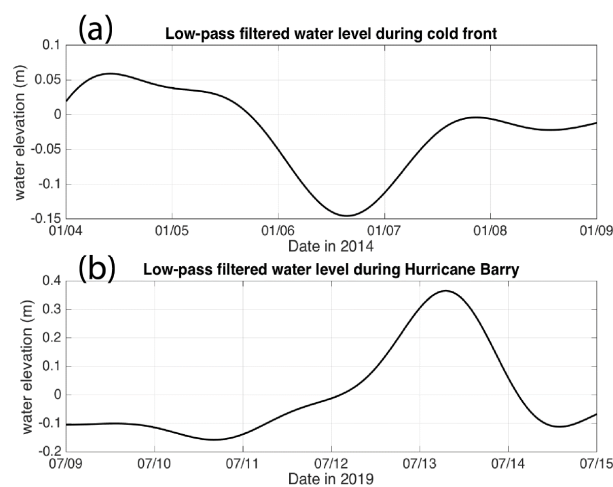

Figure 5. Water level variation during different weather types. (**a**) a cold front event and (**b**) Hurricane Barry.

Figure 6 shows the surface (Figure 6a) and bottom (Figure 6b) flows at 1200 UTC on 5 January 2014 before cold front passage when southerly wind dominated (with maximum magnitude of about 3 m/s). Flows inside the bay were in the wind's direction, flowing from south to north. Shallower and surface water had a larger magnitude of flows. Surface and bottom flows were unidirectional, while surface flow had a larger magnitude. After the cold front's passage (Figure 6c,d), when northerly wind dominated (maximum magnitude of 13.5 m/s), flows inside the bay were also in the direction of the wind, flowing from north to south. However, there existed a strong return flow in the middle of the bay where it had a greater water depth, which is consistent with previous studies in many systems: currents for shallower water tends to move in the direction of wind, whereas against the wind's direction for the region with a greater water depth (e.g., [49,56]). Again, surface and bottom flows were mostly uniform, except that surface flow had a larger magnitude. This is because bottom flow is decreased by bottom friction.

Figure 7 shows the surface (Figure 7a,c) and bottom (Figure 7b,d) flows prior (Figure 7a,b) and after (Figure 7c,d) Hurricane Barry's landfall. During Hurricane Barry, wind was rotating clockwise. Before Hurricane Barry's landfall, wind in the northern quadrant was dominating (with magnitude of 10 m/s). As a consequence, both surface and bottom currents were flowing in the direction of wind, from north to south in the shallow water region. An apparent returning flow against the wind's direction occurred in the deeper water region. After the landfall of Hurricane Barry, southerly wind dominated with the magnitude reaching 14.5 m/s. The surface and bottom flow in shallower water were flowing in the direction of the wind, moving from south to north, while in the deeper water region,

they were flowing against the direction of wind, moving from north to south. Similarly, surface and bottom flows were mostly unidirectional, except that the surface flow had a larger magnitude.
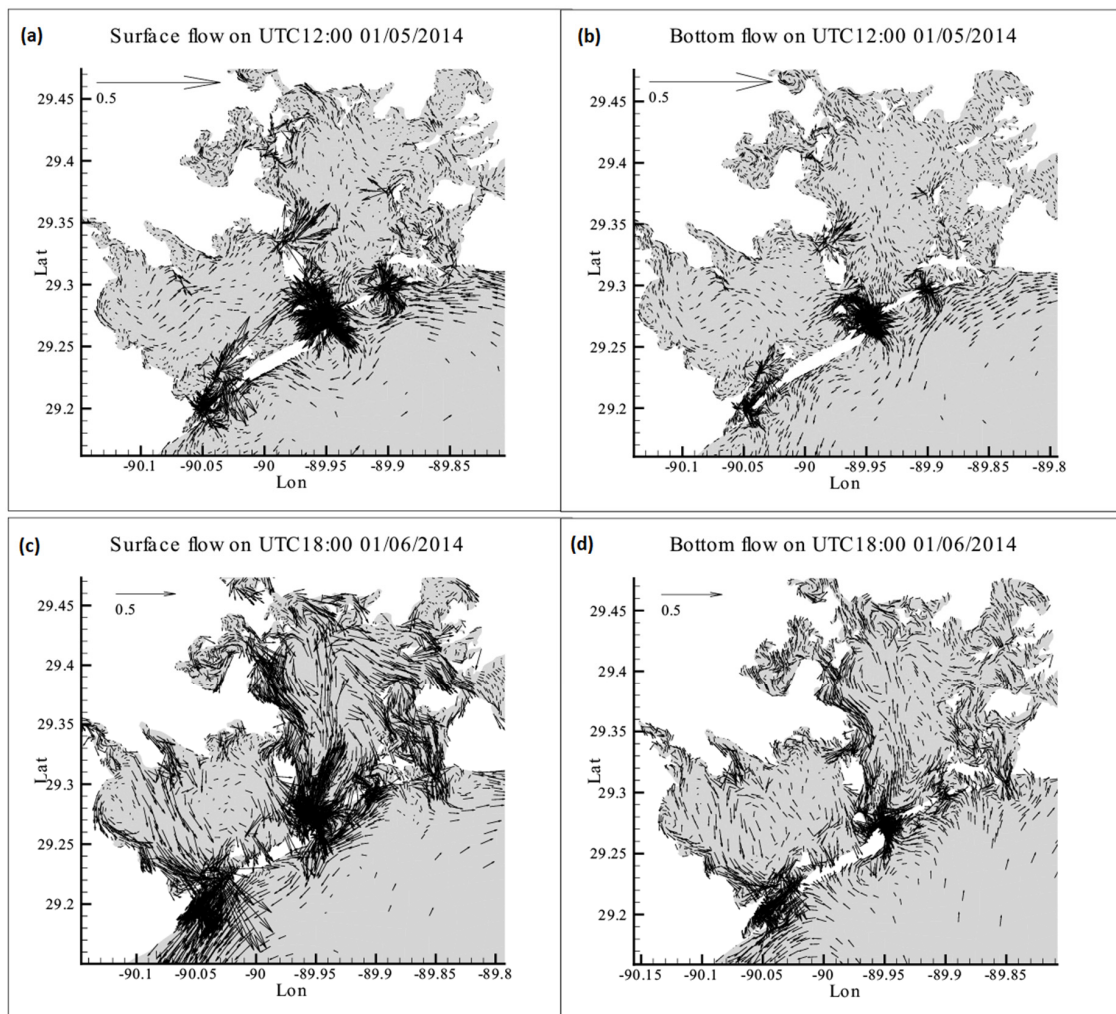

Figure 6. Surface and bottom flows influenced by the cold front event in January 2014. (**a**,**b**) are surface and bottom flows on 1200 UTC, 5 January 2014; (**c**,**d**) are surface and bottom flows on 1800 UTC, 1 January 2014.

4.2. Water Volume Transport

To examine the water transport through multiple inlets, water volume fluxes are calculated using the following equation [50]:

$$V(t)|_\Gamma = \int_{-H}^{\varsigma} (\int_0^L V_n(x,y,z,t)|_\Gamma d\xi)dz, \tag{9}$$

where V is the water volume flux in cubic meters per second. Γ is the transect perpendicular to the along-channel direction, H is the water depth, and ζ is the surface elevation. $V_n(x,y,z,t)$ is the low-pass filtered along-channel velocity in different water depths. A positive sign means water is transported into Barataria Bay.

Figure 8 shows the volume flux through Caminada Pass, Barataria Pass, Pass Abel, and Quatre Bayou. Positive value means water is flowing into the bay, while negative values means water is flowing out of the bay. During the cold front event in January 2014, the results indicate that water

volume flux through Barataria Pass was the largest. Before cold front passage at 0000 on 6 January, water was flowing inside the bay through Caminada Pass and Quatre Bayou, while it was transported out of the bay through Barataria Pass and Pass Abel, which is consistent with mode 2a in Li et al. [50] under southerly wind. After the cold front's passage, as wind changed its direction from the south quadrants to north quadrants, volume flux through the four inlets began to decrease, then started to flow into the bay. Interestingly, volume flux changed the sign at different time stages: volume flux through Barataria Pass changed its sign first, followed by Pass Abel, Caminada Pass, and Quatre Bayou at last, which means there was a period (from 2000 UTC on 6 January to 0000 UTC on 7 January) when water was flowing out of the bay through Barataria Pass, while flowing inside of the bay through the other three inlets. From 0000 UTC on 7 January, water was transported into the bay through both Barataria Pass and Pass Abel, but it transported out of the bay through the other inlets, which is consistent with mode 2b in Li et al. [50] under northerly wind.
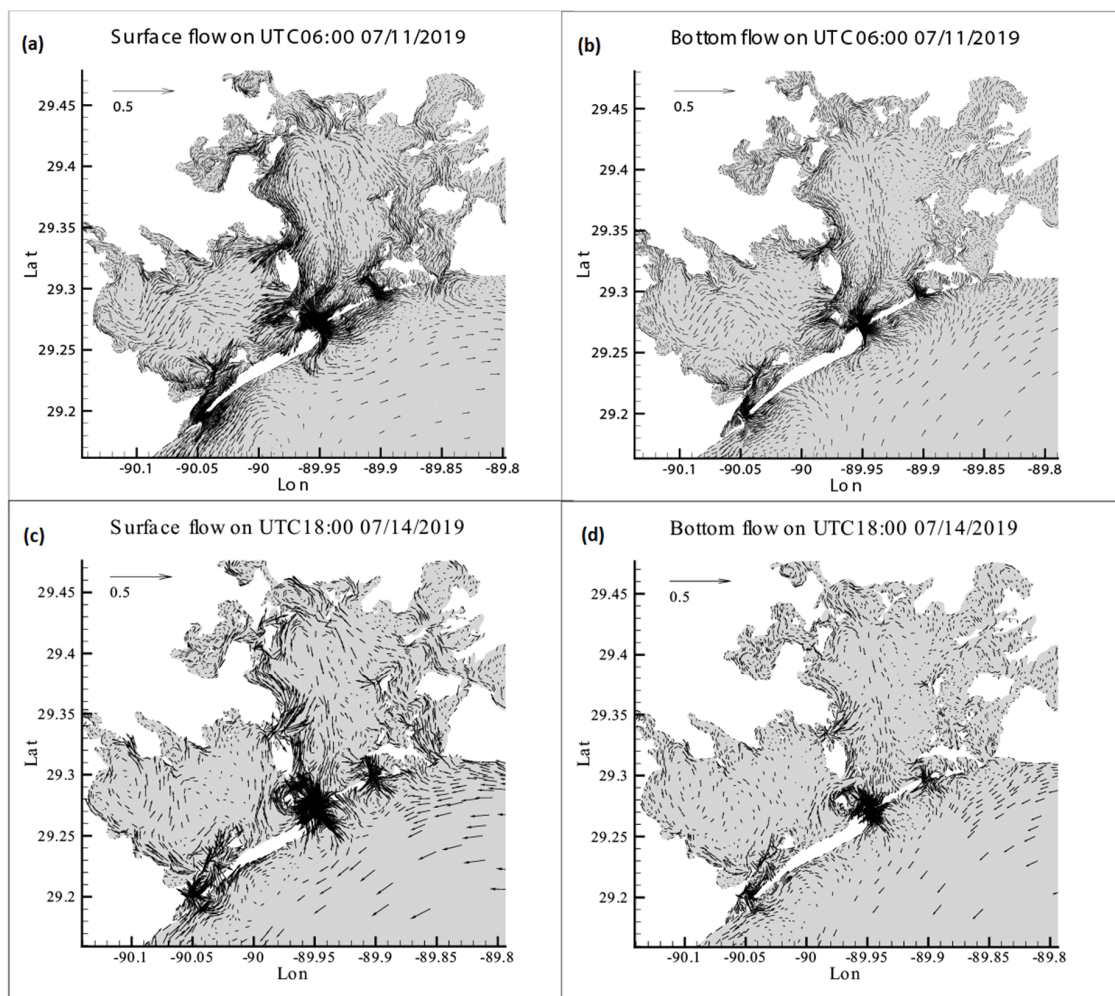

Figure 7. Surface and bottom flows under Hurricane Barry in 2019. (**a**,**b**) are surface and bottom flows on 0600 UTC, 11 July 2019; (**c**,**d**) are surface and bottom flows on 1800 UTC, 14 July 2019.

During Hurricane Barry, wind changed direction from the northern quadrants to southern quadrants. Therefore, the volume flux changed its sign after Barry's landfall on 13 July 2019, flowing into the bay through Barataria Pass, Pass Abel, and Quatre Bayou at first, then flowing out of the bay through these inlets afterwards. Note that Caminada Pass had the opposite condition: water was flowing out of the bay and then into the bay after Barry's landfall. This pattern is not included in any mode in cold front-induced flows [50]. Obviously, the mode of hurricane-induced flows can be different from that due to cold fronts. Before Barry's landfall, Pass Abel had the largest inward flux

under northerly wind, and after Barry's landfall, Barataria Pass had the largest outward flux with a magnitude reaching 2500 m³/s, which was about 4 times of that induced by the cold front.
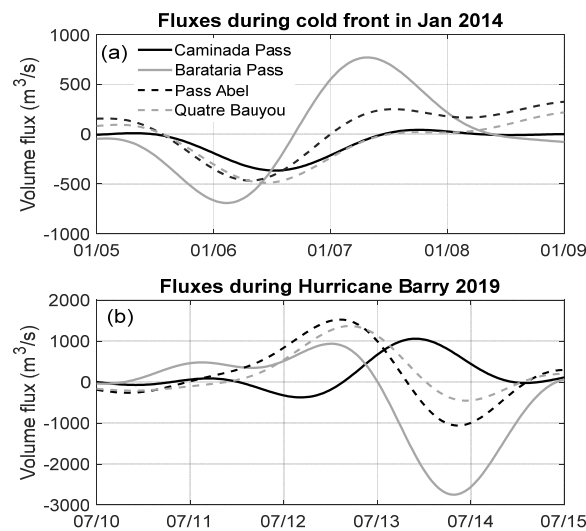

Figure 8. Volume flux through four inlets. (**a**) are fluxes in four passes during cold front, (**b**) are fluxes in four passes during Hurricane Barry.

5. Conclusions

Cold fronts and hurricanes have different wind patterns, and temporal and spatial characteristics: cold fronts usually have abrupt changes in wind direction (from southern quadrants to northern quadrants) before and after the frontal passage, with several hours to 3 days in duration, and 2000–3000 km length of front and a narrow width (less than 10 km) of the front. However, a hurricane has a radius of maximum wind (30–50 km) larger than the width of the frontal zone, and with a longer impact period of about a few days to a week, stronger maximum wind, and a rotating wind. Due to these differences, a cold front is more likely to result in a trough in water level post front, while hurricane tends to produce a more significant storm surge even severe inundation. The maximum of the variation in water level caused by Hurricane Barry was about 3 times of that caused by a cold front. The ratio is variable at different locations relative to the location of landfall.

Surface and bottom flows inside the Barataria bay have unidirectional movement except that surface flow has a larger magnitude. Currents tend to flow in the direction of wind in the shallower water region, but against the direction of wind in the deeper water region, resulting in a returning flow in the middle of bay. Water is transported out of the bay after a cold front passage. However, it is transported into the bay after Hurricane Barry's landfall. Volume flux through four inlets of Barataria Pass follows two EOF modes found by Li et al. [50] under a cold front event, in which water tends to be transported out of (into) the bay through Barataria Pass and Pass Abel during southerly (northerly) wind and into (out of) the bay through Caminada Pass and Quatre Bayou under southerly (northerly) wind. However, the volume flux through the four inlets of Barataria Bay shows different pattern under Hurricane Barry: water is flowing into (out of) the bay through Barataria Pass, Pass Abel, and Quatre Bayou under northerly (southerly) wind. The flux is the opposite through Caminada Pass, which is flowing out of (into) the bay during southerly (northerly) wind. The maximum water volume flux induced by hurricane is about 4 times that induced by a cold front event, indicating that the influence of four cold fronts is comparable with one hurricane event.

Author Contributions: Methodology, C.L.; validation, W.H.; formal analysis, W.H.; writing—original draft preparation, W.H.; writing—review and editing, C.L.; project administration, C.L. All authors have read and agreed to the published version of the manuscript.

Conflicts of Interest: The authors declare no conflict of interest.

References

1. Penland, S.; Roberts, H.H.; Williams, S.J.; Sallenger, A.H., Jr.; Cahoon, D.R.; Davis, D.W.; Groat, C.G. Coastal Land Loss in Louisiana. In *Gulf Coast Association of Geological Societies Transactions*; GCAGS: Lafayette, LA, USA, 1990; Volume 40, pp. 685–699.
2. Britsch, L.D.; Dunbar, J.B. Land loss rates: Louisiana coastal plain. *J. Coast. Res.* **1993**, *9*, 324–338.
3. Roberts, H.H. Dynamic Changes of the Holocene Mississippi River Delta Plain: The Delta Cycle. *J. Coast. Res.* **1997**, *13*, 605–627.
4. Barras, J.; Beville, S.; Britsch, D.; Hartley, S.; Hawes, S.; Johnston, J.; Kemp, P.; Kinler, Q.; Martucci, A.; Porthouse, J.; et al. Historical and Projected Coastal Louisiana Land Changes: 1978–2050. In *U.S. Geological Survey Scientific Investigations*; U.S. Geological Survey: Reston, VA, USA, 2003.
5. Penland, S.; Connor, P.F., Jr.; Beall, A.; Fearnley, S.; Williams, S.J. Changes in Louisiana's Shoreline: 1855–2002. *J. Coast. Res.* **2005**, *44*, 7–39.
6. Palaseanu-Lovejoy, M.; Kranenburg, C.; Barras, J.A.; Brock, J.C. Land Loss Due to Recent Hurricanes in Coastal Louisiana, USA. *J. Coast. Res.* **2013**, *63*, 97–109. [CrossRef]
7. Harris, D.L. Tides and Tidal datums in the United States. In *Special Reports*; U.S. Army Corps of Engineers: Washington, DC, USA, 1981; Volume 7, p. 382.
8. Forbes, M.J. Hydrologic investigations of the lower Calcasieu River, Louisiana. In *Water Resources Investigations Report 87-4173*; U.S. Geological Survey: Reston, VA, USA, 1988; p. 61.
9. Stone, G.W.; Liu, B.; Pepper, D.A.; Wang, P. The importance of extratropical and tropical cyclones on the short-term evolution of barrier islands along the northern Gulf of Mexico, USA. *Mar. Geol.* **2004**, *210*, 63–78. [CrossRef]
10. Khalil, S.M.; Lee, D.M. Restoration of isles dernieres, Louisiana: Some reflections on morphodynamic approaches in the Northern Gulf of Mexico to conserve coastal/marine systems. *J. Coast. Res.* **2006**, *39*, 65–71.
11. Day, J.W., Jr.; Boesch, D.F.; Clairain, E.J.; Kemp, G.P.; Laska, S.B.; Mitsch, W.J.; Orth, K.; Mashriqui, H.; Reed, D.J.; Shabman, L.; et al. Restoration of the Mississippi Delta: Lessons from Hurricanes Katrina and Rita. *Science* **2007**, *315*, 1679–1684. [CrossRef]
12. Morton, R.A. Historical Changes in the Mississippi-Alabama Barrier-Island Chain and the Roles of Extreme Storms, Sea Level, and Human Activities. *J. Coast. Res.* **2008**, *24*, 1587–1600. [CrossRef]
13. Otvos, E.G.; Carter, G.A. Hurricane Degradation-Barrier Development Cycles, Northeastern Gulf of Mexico: Landform Evolution and Island Chain History. *J. Coast. Res.* **2008**, *24*, 463–478. [CrossRef]
14. Morton, R.A.; Barras, J.A. Hurricane Impacts on Coastal Wetlands: A Half-Century Record of Storm-Generated Features from Southern Louisiana. *J. Coast. Res.* **2011**, *27*, 27–43. [CrossRef]
15. Dingler, J.R.; Reiss, T.E.; Plant, N.G. Erosional Patterns of the Isles Dernieres, Louisiana, in Relation to Meteorological Influences. *J. Coast. Res.* **1993**, *9*, 112–125.
16. Houston, S.H.; Shaffer, W.A.; Powell, M.D.; Chen, J. Comparisons of HRD and SLOSH surface wind fields in hurricanes: Implications for storm surge modeling. *Weather Forecast.* **1999**, *14*, 671–686. [CrossRef]
17. Hubbert, G.D.; McInnes, K.L. A storm surge model for coastal planning and impact studies. *J. Coast. Res.* **1999**, *15*, 168–185.
18. Peng, M.; Xie, L.; Pietrafesa, L.J. A numerical study of storm surge and inundation in the Croatan–Albemarle–Pamlico Estuary System. *Estuar. Coast. Shelf Sci.* **2004**, *59*, 121–137. [CrossRef]
19. Peng, M.; Xie, L.; Pietrafesa, L.J. Tropical cyclone induced asymmetry of sea level surge and fall and its presentation in a storm surge model with parametric wind fields. *Ocean Model.* **2006**, *14*, 81–101. [CrossRef]
20. Xia, M.; Xie, L.; Pietrafesa, L.J.; Peng, M. A numerical study of storm surge in the Cape Fear River Estuary and adjacent coast. *J. Coast. Res.* **2008**, *24*, 159–167. [CrossRef]

21. Chuang, W.S.; Wiseman, W.J., Jr. Coastal sea level response to frontal passages on the Louisiana–Texas Shelf. *J. Coast. Res.* **1983**, *88*, 2615–2620. [CrossRef]

22. Siadatmousavi, S.M.; Jose, F. Winter storm-induced hydrodynamics and morphological response of a shallow transgressive shoal complex: Northern Gulf of Mexico. *Estuar. Coast. Shelf Sci.* **2015**, *154*, 58–68. [CrossRef]

23. Walker, N.D.; Hammack, A.B. Impacts of Winter Storms on Circulation and Sediment Transport: Atchafalaya-Vermilion Bay Region, Louisiana, USA. *J. Coast. Res.* **2000**, *16*, 996–1010.

24. Steyer, G.D.; Perez, B.C.; Piazza, S.; Suir, G. Potential consequences of saltwater intrusion associated with hurricanes Katrina and Rita. *Sci. Storms* **2005**, *2007*, 137–145.

25. Mulrennan, M.E.; Woodroffe, C. Saltwater intrusion into the coastal plains of the Lower Mary River, Northern Territory, Australia. *J. Environ. Manag.* **1998**, *54*, 169–188. [CrossRef]

26. Pezeshki, S.R.; Delaune, R.D.; Patrick, W.H., Jr. Flooding and saltwater intrusion: Potential effects on survival and productivity of wetland forests along the U.S. Gulf Coast. *For. Ecol. Manag.* **1990**, *33–34*, 287–301. [CrossRef]

27. Neubauer, S.C. Ecosystem Responses of a Tidal Freshwater Marsh Experiencing Saltwater Intrusion and Altered Hydrology. *Estuaries Coasts* **2013**, *36*, 491–507. [CrossRef]

28. Xue, L.; Li, X.; Yan, Z.; Zhang, Q.; Ding, W.; Huang, X.; Tian, B.; Ge, Z.; Yin, Q. Native and non-native halophytes resiliency against sea-level rise and saltwater intrusion. *Hydrobiologia* **2018**, *806*, 47–65. [CrossRef]

29. Fritz, H.M.; Blount, C.; Sokoloski, R.; Singleton, J.; Fuggle, A.; McAdoo, B.G.; Moore, A.; Grass, C.; Tate, B. Hurricane Katrina storm surge distribution and field observations on the Mississippi Barrier Islands. *Estuar. Coast. Shelf Sci.* **2007**, *74*, 12–20. [CrossRef]

30. Williams, H.F.L. Stratigraphy, Sedimentology, and Microfossil Content of Hurricane Rita Storm Surge Deposits in Southwest Louisiana. *J. Coast. Res.* **2009**, *25*, 1041–1051. [CrossRef]

31. Williams, H.F.L.; Flanagan, W.M. Contribution of Hurricane Rita Storm Surge Deposition to Long-Term Sedimentation in Louisiana Coastal Woodlands and Marshes. *J. Coast. Res.* **2009**, *56*, 1671–1675.

32. Ebersole, B.A.; Westerink, J.J.; Bunya, S.; Dietrich, J.C.; Cialone, M.A. Development of storm surge which led to flooding in St. Bernard Polder during Hurricane Katrina. *Ocean Eng.* **2010**, *37*, 91–103. [CrossRef]

33. Niedoroda, A.W.; Resio, D.T.; Toro, G.R.; Divoky, D.; Das, H.S.; Reed, C.W. Analysis of the coastal Mississippi storm surge hazard. *Ocean Eng.* **2010**, *37*, 82–90. [CrossRef]

34. Rego, J.L.; Li, C. On the importance of the forward speed of hurricanes in storm surge forecasting: A numerical study. *Geophys. Res. Lett.* **2009**, *36*, L07609. [CrossRef]

35. Rego, J.L.; Li, C. On the receding of storm surge along Louisiana's low-lying coast. *J. Coast. Res.* **2009**, *SI56*, 1045–1049.

36. Li, C.; Weeks, E.; Rego, J.L. In situ measurements of saltwater flux through tidal passes of Lake Pontchartrain estuary by Hurricanes Gustav and Ike in September 2008. *Geophys. Res. Lett.* **2009**, *36*, L19609. [CrossRef]

37. Li, C.; Weeks, E.; Blanchard, B.W. Storm surge induced flux through multiple tidal passes of Lake Pontchartrain estuary during Hurricanes Gustav and Ike. *Estuar. Coast. Shelf Sci.* **2010**, *87*, 517–525. [CrossRef]

38. Shuckburgh, E.; Mitchell, D.; Stott, P. Hurricanes Harvey, Irma and Maria: How natural were these 'natural disasters'? *Weather* **2017**, *72*, 353–354. [CrossRef]

39. Li, C.; Weeks, E.; Milan, B.; Huang, W.; Wu, R. Weather Induced Transport through a Tidal Channel Calibrated by an Unmanned Boat. *J. Atmos. Ocean. Technol.* **2018**, *35*, 261–279. [CrossRef]

40. Keen, T.R. Waves and currents during a winter cold front in the Mississippi Bight, Gulf of Mexico: Implications for barrier island erosion. *J. Coast. Res.* **2002**, *18*, 6220636.

41. Keen, T.R.; Stavn, R.H. Hydrodynamics and marine optics during cold fronts at Santa Rosa Island, Florida. *J. Coast. Res.* **2012**, *28*, 1073–1087. [CrossRef]

42. Warner, J.C.; Butman, B.; Dalyander, P.S. Storm-driven sediment transport in Massachusetts Bay. *Cont. Shelf Res.* **2008**, *28*, 257–282. [CrossRef]

43. Perez, B.C.; Day, J.W., Jr.; Rouse, L.J.; Shaw, R.F.; Wang, M. Influence of Atchafalaya River Discharge and Winter Frontal Passage on Suspended Sediment Concentration and Flux in Fourleague Bay, Louisiana. *Estuarine Coast. Shelf Sci.* **2000**, *50*, 271–290. [CrossRef]

44. Kineke, G.C.; Higgins, E.E.; Hart, K.; Velasco, D. Fine-sediment Transport Associated with Cold-front passages on the shallow shelf, Gulf of Mexico. *Cont. Shelf Res.* **2006**, *26*, 2073–2091. [CrossRef]

45. Siadatmousavi, S.M.; Allahdadi, M.N.; Chen, Q.; Jose, F.; Roberts, H.H. Simulation of wave damping during a cold front over the muddy Atchafalaya Shelf. *Cont. Shelf Res.* **2012**, *47*, 165–177. [CrossRef]

46. Henrie, K.; Valle-Levinson, A. Subtidal variability in water levels inside a subtropical estuary. *J. Geophys. Res. Oceans* **2014**, *119*, 7483–7492. [CrossRef]

47. Murphy, P.; Waterhouse, A.F.; Hesser, T.J.; Penko, A.M.; Valle-Levinson, A. Subtidal flow and its variability at the entrance to a subtropical lagoon. *Cont. Shelf Res.* **2009**, *29*, 2318–2332. [CrossRef]

48. Sepulveda, H.H.; Valle-Levinson, A.; Framinan, M.B. Observations of subtidal and tidal flow in the Rio de la Plata Estuary. *Cont. Shelf Res.* **2004**, *24*, 509–525. [CrossRef]

49. Lin, J.; Li, C.; Boswell, K.; Kimball, M.; Rozas, L. Examination of winter circulation in a northern Gulf of Mexico estuary. *Estuaries Coasts* **2016**, *39*, 879–899. [CrossRef]

50. Li, C.; Huang, W.; Milan, B. Atmospheric Cold Front Induced Exchange Flows through a Microtidal Multi-inlet Bay: Analysis using Multiple Horizontal ADCPs and FVCOM Simulations. *J. Atmos. Ocean. Technol.* **2019**, *36*, 443–472. [CrossRef]

51. Li, C.; Huang, W.; Wu, R.; Sheremet, A. Weather induced quasi-periodic motions in estuaries and bays: Meteorological tide. *China Ocean Eng.* **2020**, *34*, 299–313. [CrossRef]

52. Chen, C.; Liu, H.; Beardsley, R.C. An unstructured grid, finite-volume, three dimensional, primitive equation ocean model: Application to coastal ocean and estuaries. *J. Atmos. Ocean. Technol.* **2003**, *20*, 159–186. [CrossRef]

53. Mellor, G.L.; Yamada, T. Development of a turbulence closure model for geophysical fluid problem. *Rev. Geophys. Space Phys.* **1982**, *20*, 851–875. [CrossRef]

54. Padman, L.; Erofeeva, S. A Barotropic Inverse Tidal Model for the Arctic Ocean. *Geophys. Res. Lett.* **2004**, *31*. [CrossRef]

55. Wu, H.; Zhu, J.R.; Shen, J.; Wang, H. Tidal modulation on the Changjiang River plume in summer. *J. Geophys. Res.* **2011**, *116*. [CrossRef]

56. Huang, W.; Li, C. Cold Front Driven Flows Through Multiple Inlets of Lake Pontchartrain Estuary. *J. Geophys. Res. Ocean.* **2017**, *122*, 8627–8645. [CrossRef]